Economical Chemical Synthesis and characterization of multifunctional Bi36Fe2O57polycrystalline Ceramic catalyst

Manish Kumar Verma
IIT BHU: Indian Institute of Technology BHU Varanasi
Vinod Kumar
IIT BHU: Indian Institute of Technology BHU Varanasi
Upakar Patel
IIT BHU: Indian Institute of Technology BHU Varanasi
Vishnu Shankar Rai
IIT BHU: Indian Institute of Technology BHU Varanasi
Dinesh Prajapati
IIT BHU: Indian Institute of Technology BHU Varanasi
Arup Kumar De
IIT BHU: Indian Institute of Technology BHU Varanasi
Aditya Kumar Prajapati
IIT BHU: Indian Institute of Technology BHU Varanasi
Kedar sahoo
IIT BHU: Indian Institute of Technology BHU Varanasi
Tapas Das
IIT BHU: Indian Institute of Technology BHU Varanasi
N.B. Singh
University of Maryland Baltimore County
K. D. Mandal (kdmandal.apc@iitbhu.ac.in)
Indian Institute of Technology Banaras Hindu University: Indian Institute of Technology BHU Varanasi

---

Research Article

Keywords: XRD, Microstructural studies, Photocatalytic Properties, Cyclic Voltammetry, Dielectric properties.

Posted Date: August 3rd, 2022

DOI: https://doi.org/10.21203/rs.3.rs-1861487/v1

Abstract

Polycrystalline $Bi_{36}Fe_2O_{57}$ (BFO) ceramic was prepared by an economical chemical route. The X-ray powder diffraction analysis shows the formation of single-phase BFO ceramic. Nanosized formation of BFO ceramic particles was characterized by XRD as well as TEM and had particle size 76 ± 10 nm range. The sillenite type $Bi_{36}Fe_2O_{57}$ shows better photocatalytic activity for the methylene blue (MB) dye degradation under visible light exposure than the perovskite-based $BiFeO_3$ due to the low band gap(1.8eV) of the former. The photocatalytic mechanism of MB degradation over $Bi_{36}Fe_2O_{57}$ ceramic can be explained by the Langmuir-Hinshelwood model which reflects the adsorption-controlled photocatalytic process.

1. Introduction

In modern times, water pollution is a dangerous threat to humans and animals. Water and wastewater removal from the textile industry affects the environment significantly and seriously threatens human health(Rawat et al. 2007). According to a joint report by UNICEF and FAO, it is calculated that there are nearly 780 million people who hardly get clean drinking water. It has been reported that around 37.7 million people are affected by water-borne diseases every year, 1.5 million children are likely to die from diarrhea alone, and 73 million working people die due to water-borne diseases each year(Yao et al. 2003; Zhang et al. 2009).Several manufacturing industries e.g., textile,cosmetics, leather,plastic, pulp, paper, paint, and food processing industries use dyes to color their products and produce millions of tons of dyes each year(Wang et al. 2007; Verma et al. 2020). There are so many types of toxic contaminants like carcinogenic dyes, wastewater, and toxic gases present in our environment. Polluted water is responsible for two-thirds of all illnesses in developing countries. So to decrease the illnesses which affect human health caused by polluted water, we have to find new processes and materials which remove these toxic dyes from wastewater and this is a major challenge for the scientific community these days(Chu et al. 2003; Auta and Hameed 2014; Verma et al. 2020). As of now, photocatalysis is among the powerful technologies with the advantage of low energy consumption, and a facile and environmentally non-violent process (Chu et al. 2003; Kant 2012; Auta and Hameed 2014; Verma et al. 2020). In the old days, TiO_2 was generally used as photocatalytic semiconductor oxide. Recently, scientists have devised novel photocatalytic materials that can be produced in two ways-One is based on the alteration of TiO_2 compositions, while the other consists of a set of processes to find the novel metals and non-metals, composite materials, and semiconductor oxides with photocatalytic activity. TiO_2 is classical photocatalytic material, which works gradually and is less effective due to the high band gap, but some modified advanced TiO_2 materials which also show fast photocatalytic properties and clean measure amount of wastewater(Liquid et al. 2015; Deng et al. 2018; Singh et al. 2021). Bismuth-containing sillenite, and perovskite-type materials have been found to display photocatalytic properties e.g., sillenite type $Bi_{12}TiO_{20}$, $Bi_{25}FeO_{40,\text{ and }}$ $Bi_{35}Fe_2O_{57}$ ceramics. $Bi_{12}TiO_{20}$ exhibits photocatalytic activities and good dielectric properties. The general class of sillenite type $Bi_{12}MO_{20\pm\delta}$ (where, M = Fe, Ni, Ti, Al, etc.) acts as profound catalysts and has severely grasped the attention of various scientists because of its

phenomenal electrical and optical properties. Earlier, the photodegradation through $Bi_{25}FeO_{40}$ was found to be efficient due to the smaller band gap. $BiFeO_3$, $Bi_2Fe_4O_9$, and $Bi_{12}TiO_{20}$were also synthesized by the chemical route and sol-gel method and these compounds also showed photocatalytic degradation. However ,in the current study of the bismuth-related compound, sillenite-type compound $Bi_{36}Fe_2O_{57}$ shows excellent photocatalytic properties as well as electrical properties(Verma et al. 2020; Singh et al. 2021). In this work, single-phase $Bi_{36}Fe_2O_{57}$(BFO) was prepared by the sol-gel method.

2. Experimental

2.1. Material Synthesis

Bismuth nitrate $Bi(NO_3)_3.6H_2O$ (99% Merck, India) and iron nitrate $Fe(NO_3)_3.9H_2O$ were used as starting ingredients in a chemical process to create $Bi_{36}Fe_2O_{57}$. Separately, the stoichiometric amounts of iron and bismuth nitrates were dissolved in deionized water and combined in a beaker. A suitable amount of glycine (C_2H_5 (NO_2), 99% Merck, India), equivalent to the metal ions, was dissolved in de-ionized water and added to the solution combination. To evaporate the water, the resulting mixture was heated on a hot plate at 70 to 80°C with a magnetic stirrer. Upon ignition, a fluffy mass that burns with a sooty flame is produced. Using a mortar and pestle, the resultant fluffy material was ground into a fine powder. The resulting powder was dried. In the electrical muffle furnace, the resulting dry powder was calcined at 600°C for 6 hours. Finally, the calcined material was sintered at 800°C for 8 hours and used for several physicochemical characterizations, including microstructural characterization by XRD, SEM, TEM, EDX, cyclic voltammetry, and photocatalytic activity.

2.2. Materials and fabrication of electrodes

Acetylene black (AB), Nafion solution, and iso-propanol were purchased from Alfa Aesar. The individual electrode was fabricated by mixing 5 mg of active material, 0.625 mg of AB, 0.2 mL of isopropanol, 12μLNafion, and impregnating the dispersion on glossy carbon paper having an area of 1 cm^2 and then drying at normal atmospheric conditions. Copper wire was connected to the electrode by silver glue which worked like a current collector.

2.3. Electrochemical characterization

To examine the electrochemical responses of the created electrodes, Versastat 3 was employed. The built systems were subjected to cyclic voltammetry (CV) utilising a three-electrode mechanism. A reference electrode (Ag/AgCl), working electrode (fabricated system/active substance), and counter electrode made up the three electrode systems (Platinum). In the three-electrode setup, the working electrode had an active mass loading of 2 $mg.cm^{-2}$. The stable potential range was discovered to be 0 V to 1 V when CV was conducted at a rate of 5 mV/s. The three-electrode devices were subjected to electrochemical impedance spectroscopy (EIS) at 10 mV AC amplitude across 100 kHz to 0.01 Hz frequency. The electrolyte used for the electrochemical tests was a 1M KOH solution.

2.4. Photocatalytic experiments

The photodegradation of Rhodamine B (RhB) was performed to evaluate the photocatalytic activity of the synthesized material. The experiment was performed in a homemade photocatalytic chamber using four cool white LED bulbs. In a 4 ml standard quartz cuvette, a 2.3 ml aqueous solution of RhB (3.5 mg/L) and 0.1 mg catalyst were mixed with proper homogenous dispersion. Then, the whole mixture was stirred for 10 minutes in the dark to ensure the adsorption-desorption equilibrium between the catalyst and respective reactant (RhB). Only after that, the cuvette was allowed to keep under visible light irradiation, and the UV-Vis absorption spectrum was recorded on the UV-Vis spectrophotometer (Agilent Cary 60 model) after every 5 minutes time interval. The photocatalytic scavenging experiment was executed in the same way, only adding scavenger after dark stirring.

The optical band gap of the BFO nanoparticle was evaluated from the observed diffuse reflectance spectra. Reflectance spectra were recorded with the help of a balanced deuterium-halogen source (DH 2000 BAL, Ocean Optics) with a 210–2500 nm spectral range.

3. Material Characterization

Rigaku Miniflex 600, Japan, X-ray powder diffractometer with Cu-Kα X-ray source(λ=1.54Ǻ) was used for the powder X-ray diffraction of the prepared $Bi_{36}Fe_2O_{57}$ ceramic to analyze its phase assembly and crystallinity. SEM(ZEISS, model EVO–18 research; Germany) and EDS(Oxford instrument; USA) were performed for the analysis of grain size distribution and elemental composition of the prepared ceramic, respectively. Moreover, analysis of nanostructure and particle size was performed with the help of TEM (FEI TECNAI G^2 20 TWIN; USA). Further, with the help of an LCR meter(PSM 1735, NumetriQ 4th Ltd. U.K.), the temperature and frequency-dependent dielectric studies of the prepared sample were performed.DH 2000 BAL, Ocean Optics, Diffuse Reflectance Spectrometer (spectral range- 210-2500nm) was utilized to record the reflectance spectra and so to determine the optical bandgap energy of $Bi_{36}Fe_2O_{57}$nanoparticles.

4. Results And Discussion

4.1. X-Ray Diffraction (XRD) analysis:

The sharp and intense peaks of $Bi_{36}Fe_2O_{57}$ ceramic are indicative of its crystalline nature. The peaks were indexed using JCPDS card No. 14-01811 for $Bi_{36}Fe_2O_{57}$, where all the peaks were well matched. This indicates the formation of single-phase $Bi_{36}Fe_2O_{57}$ ceramic. No sign of a secondary phase was observed in the prepared ceramic. The $Bi_{36}Fe_2O_{57}$nanoparticles were sintered at 800°C for 8h. The single-phase formation is possible only when the amounts of Bi and Ti are nearby to the stoichiometric ratio of the formula. Also, no major deviations were observed in the crystalline phase intensity during the sintering process.

4.2. X-ray Photoelectron Spectroscopy (XPS) studies:

The XPS studies were performed to confirm the oxidation states of each element in the $Bi_{36}Fe_2O_{57}$. The peaks for Bi, Fe, and O are shown below in Fig. 2**-** (a), (b), and (c) respectively.

For the detection of elements in the sample, a narrow range scan was used, as shown in Figs. 2(a), 2(b), and 2(c), which exhibit high-res. spectra of Bi 4f, Fe 2p, and O 1s, respectively. Figure 2(a) shows two primary balanced peaks at 158.67 and 164.01 eV, the former of which agrees to the binding energy of Bi $^4f_{5/2}$ and the letter to that of Bi $^4f_{7/2}$, suggesting that Bi in the sample largely consists of Bi $^4f_{7/2}$. It can be inferred from the XPS spectra Fig. 2(b) that Fe exists in the trivalent state of the sample. Furthermore, the spectrum revealed a satellite peak at 718.18 eV with an interval spacing of about 8 eV between Fe $^2\mathbf{p}_{3/2}$ and Fe $^2\mathbf{p}_{3/2}$ (sat.) and another satellite peak at 731.33 eV was nearly 8 eV distant from the main peak Fe $^2\mathbf{p}_{1/2}$. In theory, the oxidation of Fe causes the satellite peak to emerge alongside the main peak. Because the valance band energies of Fe^{2+} and Fe^{3+} differ, the location of the associated satellite peak differs as well. The satellite peak's position determines the type of Fe i.e., its oxidation state in the sample(Kothari et al. 2007). The Fe $^2\mathbf{p}_{3/2}$ photoelectron peak is challenging to evaluate because of the complicated chemical valance of Fe. The chemical valance of Fe is frequently determined by the peak of a satellite. The Fe^{2+} peak is always accompanied by 7.0 eV above the satellite peak. The satellite peak of Fe^{3+}appears at 5.0 eV above the principal peak, while the principal peak is 7.0 eV above it, which is the most important (Pandirengan et al. 2015). Figure 2(c) represents the O 1s spectrum with excellent resolution. The main peak located at 529.48 eV and another peak at 531.28 eV correspond to O 1s binding energy of $Bi_{36}Fe_2O_{57}$ (Wang et al. 2004).

4.3. Transmission Electron Microscopy (TEM) analysis:

The outcomes from the TEM analysis of $Bi_{36}Fe_2O_{57}$ ceramic sintered at 800°C for 8h, have been picturized in Fig. 3**(a-b)**. Figure 3**(a)** is representative of the bright field image while Fig. 3**(b)** shows the selected area electron diffraction(SAED) patterns of the $Bi_{36}Fe_2O_{57}$ ceramic. It can be inferred from both of the figures that the ceramic created using this method is nanocrystalline. From the particle size calculations, the average particle size measured was between 76 ± 10 nm. Due to their orientation in various directions, the extra dots seen in the SAED patterns originate from nearby grains and sub-grains. The appearance of lattice fringes is quite apparent from HR-TEM image in Fig. 3**(c)**which clearly defines that the material is highly crystalline with no phase separation. The measured spacing between the fringes was around 1.778Å which agrees with the (2 1 1) miller plane.

The electron diffraction patterns have been indexed based on the cubic crystal structure. The spacing between the planes (d_{hkl}) measured from SAED patterns is in good agreement with that found from the XRD analysis. This further confirms the existence of crystalline single-phase material.

4.4. Scanning Electron Microscopy (SEM) Analysis:

The grain and grain size distribution studied using SEM analysis of BFO ceramic is displayed below in Fig. 4. The bimodal distribution of grain size is evident from the figure with smaller grains of about 0.7 µm in diameter and larger grains of about 787.09 nm. The earlier literature published in this regard also reported this type of bimodal morphology of grains.

4.5. Cyclic Voltammetry (CV) :

Cyclic Voltammetry result (Fig. 5a) shows that BFO has a stability potential window of 1 Volt (0–1 V) and a current of around 2 mA was generated. There is no significant redox peak seen for BFO (Das and Verma 2020a). The plateaus are not rectangular, which reflects the pseudocapacitive nature of the material. The specific capacitance of BFO was found to be 94.5 F/g. Electrochemical Impedance Spectroscopy (EIS) was done to analyze the contribution of different components toward the overall resistance during the experiment. The equivalent series resistance (R_S) can be inferred from Nyquist plot, where it is denoted by the point of intercept about the real axis. R_S is the combination of electrolyte or solution resistance, the resistance between the electrode and current collector, intrinsic resistance existing in the composite, and resistance due to chemically inactive constituents of the composite(Sarma and Das 2021).

The charge transfer resistance (R_{CT}) can be obtained from the semi-circle's diameter in the Nyquist plot, which arises due to the abruptness in charge mobility and faradaic transitions during electrochemical reactions. BFO has a charge transfer resistance of 140 Ω given in Fig. 5**(b)**.

Figure 5**(c)**demonstrates that the impedance is decreasing with an increase in frequency for both higher and lower frequency regions. With the increase in frequency, the mobility of electrolyte ions increases resulting in less impedance(Das and Verma 2020b). Figure 5**(d)**shows that the capacitance is decreasing with an increase in frequency, which could be due to the incomplete transitions and less residence time of the electrolyte ions during electrochemical reactions(Das and Verma 2020b).

4.6. Photocatalytic activity

The photocatalytic activity of the material is evaluated by the photodegradation kinetics of RhB. Figure 6**(a)** displays the UV-Vis absorption spectra of the photodegradation of RhB using the synthesized material. The RhB can be completely removed within 25 minutes (shown in Fig. 6**(a)**). The blank experiment (without catalyst) approximately does not show any photodegradation. Figure 6**(b)** also depicts that the material can exhibit good photocatalytic activity.

Furthermore, the kinetics of the photodegradation are investigated and presented in Fig. 6**(c)**. The kinetic plot of $\ln(C_0/C)$ vs time (t) is fitted by a pseudo-first-order reaction. The reaction follows the following equation,

$\ln(C_0/C) = kt$…….(1)

Where C_0 and C are the initial and final concentrations of the RhB at irradiation time t. k is the rate constant (min^{-1}), which is the slope of the equation. The calculated rate constant of the catalyst is 0.1032 min^{-1}, and R^2 value for the fitting is 0.98. After that, the photo-generated reactive species are determined by the scavenging experiment. A particular scavenger can trap a certain reactive species. Potassium iodide (KI), isopropyl alcohol (IPA), and para-benzoquinone (PBQ) scavengers are used to trap holes (h^+), hydroxyl radical (.OH), and superoxide radical ($O_2.^-$), respectively. As shown in Fig. 6**(d)**, there are no effects on KI and IPA scavengers. Only, the PBQ decreases the reaction rate in comparison to without scavenger. Therefore, $O_2.^-$ is the main active species to control the photodegradation of RhB.

4.7. Diffuse Reflectance Spectroscopy (DRS) studies:

In contrast to the NIR area, the diffuse reflectance spectra of nanoparticles (Fig. 7) reveal substantial light absorption in the UV-Visible range. Similar to what was previously reported, the optical band gap value (E_g) of a $Bi_{36}Fe_2O_{57}$ nanoparticle is 3.54 eV, albeit this value may change depending on the nanoparticle's size and the synthesis method used to make it. Depending upon different methods used to detect the optical band gap have an important impact on the band gap value observed. In the current experiment, we used the Kubelka-Munk theory to determine the optical band gap value of $Bi_{36}Fe_2O_{57}$ nanoparticles using diffuse reflectance spectra that were acquired-

$$F(R) = \frac{\alpha}{S} = \frac{(1-R)^2}{2R}$$

F(R): Kubelka-Munk function,

α: absorption coefficient,

R: reflectance,

S: scattering factor

Equation 1 describes that the Kubelka-Munk function is proportional to the absorption coefficient.

The plot of diffuse reflectance vs wavelength may be used to compute the optical band gap, and the band gap energy is determined by where the linear rise in the curve starts. However, this approach for estimating band gap energy yields a result that is somewhat off, thus it is necessary to disclose the kind of transition (direct/indirect) during the assessment.

Absorption edge analysis was applied to find the type of transition and to determine the optical band gap represented in Eq. 2.

$\alpha h\nu = k*(h\nu - E_g)^{1/n}$ (2)

k: energy independent constant,

E_g: Optical band gap

The exponent defines the type of transition where the value of n = 2 and 1/2 for direct and indirect allowed transitions respectively. Since F(R) is proportional to α, the modified form of Eq. 2 can be represented as

$F(R)*hv = k*(hv- E_g)^{1/n}$ (3)

The exponent n in Eq. 3, can be determined from the plot of $(F(R).hv)^n$ vs. hv. The best fit to the straight line near the onset of absorption, observed for n = 1/2 recommends indirect allowed transition for the $Bi_{36}Fe_2O_{57}$ nanoparticle.

From the plot of $(F(R)*hv)^{1/2}$ vs. hv (Fig. 7) the band gap value of the prepared BFO nanoparticle is calculated to be 3.54 eV, from the extrapolation of the linear region of the curve.

4.8. Dielectric Studies:

Figure 8**(a)** shows the measured data on the frequency dependence of the dielectric constant ⍰r for sintered BFO ceramics sintered at 800°C for a period of 8 h. The values of ⍰$_r$ for BFO ceramic measured at 310 K and 100 Hz, were found as 375. As seen in Fig. 8a, the dielectric constant (⍰r) decreases in the lower frequency range while remaining constant in the higher frequency range. The dielectric constant was found high in the lower frequency region due to space charge polarization and in the higher frequency region, Rapid reversal of electric field occurs, so the dielectric constant was found lower. The value of tan δ is shown as a function of frequency. It declines smoothly in higher frequency regions, as seen in Fig. 8**(b)**. At 310 K and 100 kHz, the dielectric loss of ceramic was determined as 0.51.

5. Conclusions

The sillenite-based next-generation $Bi_{36}Fe_2O_{57}$photocatalyst was synthesized successfully through glycine assisted chemical route. For the investigation of its quality and performance, several microscopic, spectroscopic, diffraction, and electrochemical techniques such as Powder XRD, TEM, SEM, XPS, CV, DRS, and dielectric studies were performed. The photocatalytic activity and efficiency of $Bi_{36}Fe_2O_{57}$were thoroughly analyzed by photodegradation of Rhodamine B dye under UV-Visible light irradiation. By the absorption of visible light, there occurs a direct transition at 3.54eV, which makes it an efficient 3rd generation photocatalyst having a similar behavior to its $Bi_{12}MO_{20}$ isomorphs reported so far.

Declarations

Ethical Approval The experimental protocols and handling of instruments and chemicals were approved by the Ethics Committee of Indian Institute of Technology
(Banaras Hindu University) Varanasi-221005.

Consent to participate Not applicable.

Consent for publication We do give our consent to publish our data.

Competing Interests:

The work described in this manuscript, has not been published before; it is not under consideration for publication anywhere else; and publication has been approved by all co-authors and the responsible authorities at the institute(s) where the work has been carried out.

The authors declare no conflicts of interest regarding the publication of this paper.

Authors Contribution

All authors contributed to the study conception and design. Material preparation, data collection and analysis were performed by Dr. Manish Kumar Verma, Dr. Vinod Kumar, Vishnu Shankar Rai, Dinesh Prajapati Upakar Patel, Aaditya Kumar Prajapati and Tapas Das. The first draft of the manuscript was written by Arup Kumar De, Kedar Sahaoo, ,Dr. N. B. Singh and Prof. K.D. Mandal commented on previous versions of the manuscript. All authors read and approved the final manuscript.

Funding Information: *The authors declare that no funds, grants, or other support were received during the preparation of this manuscript.*

References

1. Auta M, Hameed BH (2014) Chitosan-clay composite as highly effective and low-cost adsorbent for batch and fixed-bed adsorption of methylene blue. Chem Eng J 237:352–361. https://doi.org/10.1016/j.cej.2013.09.066
2. Chu SZ, Inoue S, Wada K, et al (2003) Highly porous (TiO2-SiO2-TeO2)/Al2O3/Ti O2 composite nanostructures on glass with enhanced photocatalysis fabricated by anodization and sol-gel process. J Phys Chem B 107:6586–6589. https://doi.org/10.1021/jp0349684
3. Das T, Verma B (2020a) Effect of ruthenium based catalyst loading on the electrochemical properties of carbon xerogel. Chem Phys Lett 739:136947. https://doi.org/10.1016/j.cplett.2019.136947
4. Das T, Verma B (2020b) Polyaniline-Acetylene black-Copper cobaltite based ternary hybrid material with enhanced electrochemical properties and its use in supercapacitor electrodes. Int J Energy Res 44:934–949. https://doi.org/10.1002/er.4951
5. Deng C, Wei X, Liu R, et al (2018) Synthesis of sillenite-type bi 36 fe 2 o 57 and elemental bismuth with visible-light photocatalytic activity for water treatment
6. Kant R (2012) Textile dyeing industry an environmental hazard
7. Kothari D, Reddy VR, Gupta A, et al (2007) Study of the effect of Mn doping on the BiFeO3 system

8. Liquid OF, Deutscher RL, Fletcher S, et al (2015) Doping Effect on the Optical , Electro-optic , and Photoconductive Properties of Bi 12 MO 20 (M = Ge , Si , Ti). J Am Ceram Soc 3683:47–56. https://doi.org/10.1111/jace.12715
9. Pandirengan T, Arumugam M, Durairaj M, et al (2015) Doping Effect on the Optical , Electro-optic , and Photoconductive Properties of Bi 12 MO 20 (M = Ge , Si , Ti). J Am Ceram Soc 3683:47–56. https://doi.org/10.1111/jace.12715
10. Rawat J, Rana S, Srivastava R, Misra RDK (2007) Antimicrobial activity of composite nanoparticles consisting of titania photocatalytic shell and nickel ferrite magnetic core. Mater Sci Eng C 27:540–545. https://doi.org/10.1016/j.msec.2006.05.021
11. Sarma A, Das MK (2021) Improving the sustainable performance of Biopolymers using nanotechnology. Polym Technol Mater 60:1935–1965. https://doi.org/10.1080/25740881.2021.1937645
12. Singh S, Kumar A, Pandey SK, et al (2021) Facile synthesis of efficient heterogeneous photocatalytic and highly dielectric Bi4BaTi4O15 ceramic with remarkable applicability in the degradation of rhodamine B dye. Mater Technol 00:1–18. https://doi.org/10.1080/10667857.2021.1903137
13. Verma MK, Kumar A, Singh L, et al (2020) Bi25feo40 polycrystalline ceramic as highly efficient photocatalyst synthesised via economical chemical route. Taylor & Francis
14. Wang Y, Wei X, Shen G, et al (2007) Alkali Metal Ions-Assisted Controllable Synthesis of Bismuth Ferrites by a Hydrothermal Method. J Am Ceram Soc 90:3673–3675. https://doi.org/10.1111/j.1551-2916.2007.01952.x
15. Wang YP, Zhou L, Zhang MF, et al (2004) Room-temperature saturated ferroelectric polarization in BiFeO3 ceramics synthesized by rapid liquid phase sintering
16. Yao WF, Wang H, Xu XH, et al (2003) Sillenites materials as novel photocatalysts for methyl orange decomposition. Chem Phys Lett 377:501–506. https://doi.org/10.1016/S0009-2614(03)01209-0
17. Zhang CY, Sun HJ, Chen W, et al (2009) Hydrothermal synthesis and photo-catalytic property of Bi 25FeO40 powders. IEEE Int Symp Appl Ferroelectr 1–3. https://doi.org/10.1109/ISAF.2009.5307531

Figures

Figure 1

Powder XRD patterns of $Bi_{36}Fe_2O_{57}$ sintered at 800 ºC for 8h.

Figure 2

(a), (b),(c) high-res .XPS spectra of Bi, Fe, and O elements of $Bi_{36}Fe_2O_{57}$ Ceramic.

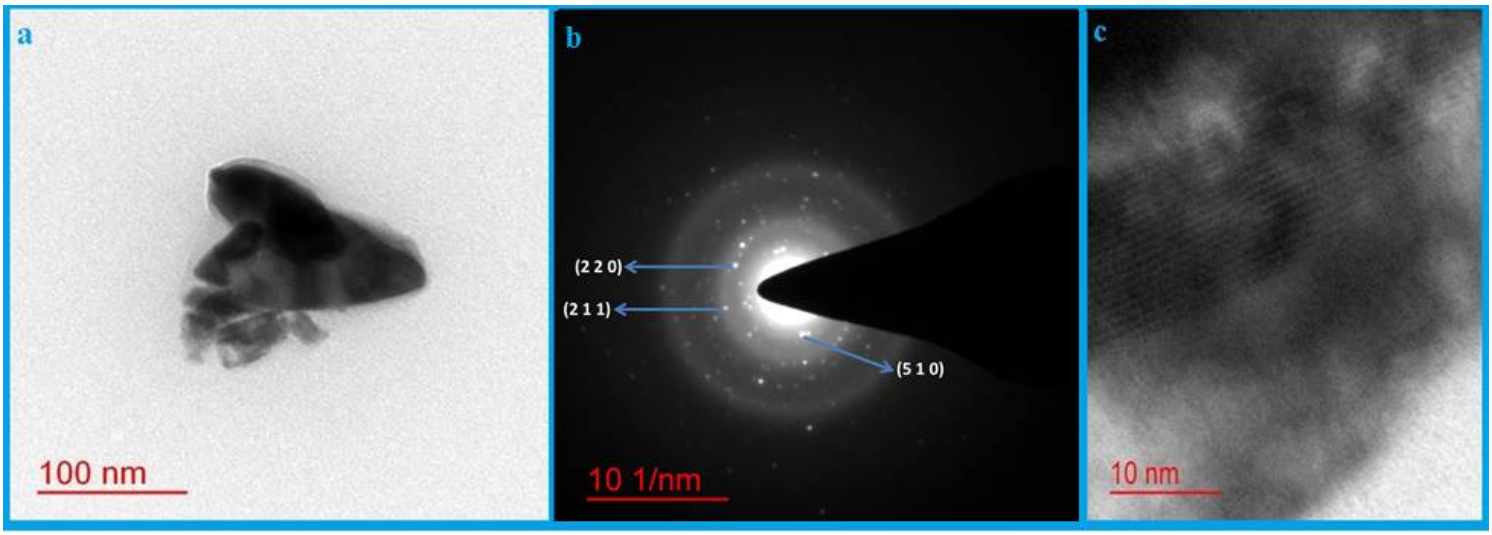

Figure 3

(a) Bright-field TEM images sintered at 800 °C and **(b)** SAED pattern **(c)** HR-TEM of $Bi_{36}Fe_2O_{57}$Ceramic.

Figure 4

SEM images of $Bi_{36}Fe_2O_{57}$ ceramic sintered at 800°C for 8h.

Figure 5

(a) Cyclic voltammetry, **(b)** Nyquist plot, **(c)** Frequency vs total impedance plot, and **(d)** Frequency vs net capacitance plot of BFO-based system

Figure 6

(a) The UV-Vis absorption spectrum of photo-degradation of RhB using synthesized material **(b)** comparative photodegradation as a function of time **(c)** kinetics plot for the degradation of RhB**(d)** Comparative photodegradation using different scavengers.

Figure 7

Diffuse reflectance spectra of BFO nanoparticles. Inset figure showing optical bandgap value of BFO nanoparticle evaluated from Kubelka-Munk theory.

Figure 8

(a) Frequency dependence of Dielectric constant ($_r$); and**(b)**tangent loss (tan of $Bi_{36}Fe_2O_{57}$ceramic at 310 K**.**